

MONTE CARLO MODELING OF LIGHT TRANSPORT IN TISSUES

Steven L. Jacques and Lihong Wang

4.1. INTRODUCTION

Monte Carlo simulations of photon propagation offer a flexible yet rigorous approach toward photon transport in turbid tissues. This method simulates the “random walk” of photons in a medium that contains absorption and scattering. The method is based on a set of rules that govern the movement of a photon in tissue. The two key decisions are (1) the mean free path for a scattering or absorption event, and (2) the scattering angle. Figure 4.1 illustrates a scattering event. At boundaries, a photon is reflected or moves across the boundary. The rules of photon propagation are expressed as probability distributions for the incremental steps of photon movement between sites of photon–tissue interaction, for the angles of deflection in a photon’s trajectory when a scattering event occurs, and for the probability of transmittance or reflectance at boundaries. Monte Carlo light propagation is rigorous yet very descriptive. However, this method is basically statistical in nature and requires a computer to calculate the propagation of a large number of photons. To illustrate how photons propagate inside tissues, a few photon paths are shown in Fig. 4.2.

The number of photons required in a simulation depends largely on the question being asked, the precision needed, and the spatial or temporal resolution desired. For example, to simply learn the total reflectance, R_t , from a tissue

STEVEN L. JACQUES AND LIHONG WANG • Laser Biology Research Laboratory, The University of Texas M.D. Anderson Cancer Center, Houston, Texas 77030.

Optical-Thermal Response of Laser-Irradiated Tissue, edited by A. J. Welch and M. J. C. van Gemert, Plenum Press, New York, 1995.

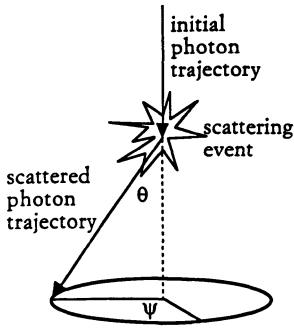


Figure 4.1. Deflection of a photon by a scattering event. The angle of deflection, θ , and the azimuthal angle, ψ , are indicated.

of specified optical properties, typically about 3,000 photons can yield a useful result. To map the spatial distribution of photons, $\phi(r,z)$, in a radially symmetric problem, at least 10,000 photons are usually required to yield an acceptable answer. To map spatial distributions in a more complex three-dimensional problem such as a finite-diameter beam irradiating a tissue with a buried blood vessel, the required photons may exceed 100,000. The main point in these introductory remarks is that Monte Carlo simulations are rigorous, yet statistical and therefore require significant computation time to achieve a specified precision and resolution. Nevertheless, the flexibility of the method makes Monte Carlo modeling a powerful tool.

Another aspect of the Monte Carlo simulations presented in this paper deserves emphasis. The simulations described here treat the photon as a neutral particle. They do not treat the photon as a wave phenomenon. Thus features such as phase and polarization are ignored. The motivation for these simulations is to predict radiant energy transport in turbid tissues. The photons are multiply scattered by most tissues and phase and polarization are quickly randomized. Although the Monte Carlo simulations can compute phase and polarization, this paper will not consider these issues.

The Monte Carlo simulations are based on macroscopic optical properties that are assumed to extend uniformly over small units of tissue volume. The

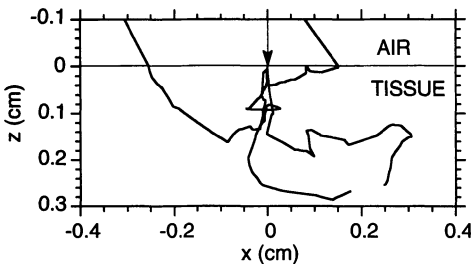


Figure 4.2. Illustration of several typical photon paths inside a semi-infinite tissue. The optical properties of the tissue are: relative refractive index 1.37, absorption coefficient 1 cm^{-1} , scattering coefficient 100 cm^{-1} , anisotropy 0.9. The coordinate can be seen in Fig. 4.7. Two of the photons are reflected back into the air. Variable step size and unweighted photons are used in this Monte Carlo simulation. Note

that some details in each path may not show well in this picture due to the limited resolution.

simulations do not treat the details of radiant energy distribution within cells, for example. Mean free paths between photon–tissue interaction sites typically range from 10–1000 μm , with 100 μm being a very typical value in the visible spectrum.¹

4.2. SAMPLING RANDOM VARIABLES

The Monte Carlo method, as its name implies (“throwing the dice”), relies on the random sampling of propagation variables from well defined probability distributions. Cashwell and Everett² provide a good reference for the principles of Monte Carlo modeling. Witt³ has also been helpful with regard to calculating photon propagation. Let us briefly review the method for “throwing the dice” in a Monte Carlo program.

Consider some random variable x which is needed by the Monte Carlo propagation equations. This variable may be the variable stepsize, s , a photon will take between photon–tissue interaction sites, or the angle of deflection, θ , a scattered photon may experience due to a scattering event. There is a probability density function, $p(x)$, which defines the distribution of x over the interval $a \leq x \leq b$, such that:

$$\int_a^b p(x) dx = 1 \quad (4.1)$$

The probability that x will fall in the interval $[a, x_1]$, such that $a \leq x \leq x_1$, is given by the distribution function, $F_x(x)$, which is defined by

$$F_x(x_1) = \int_a^{x_1} p(x) dx \quad (4.2)$$

We wish to utilize the random number generator of the computer to generate a random variable, ζ , that will specify a unique choice of x that is consistent with the probability density function $p(x)$. The probability density function for ζ is a constant, $p(\zeta) = 1$, within the interval $[0, 1]$. The corresponding probability distribution, $F_\zeta(\zeta_1)$, is defined by

$$F_\zeta(\zeta_1) = \int_0^{\zeta_1} p(\zeta) d\zeta = \zeta_1 \quad \text{for } 0 \leq \zeta_1 \leq 1 \quad (4.3)$$

These four functions, $p(x)$, $F_x(x_1)$, $p(\zeta)$, and $F_\zeta(\zeta_1)$, are illustrated in Fig. 4.3.

The key to the Monte Carlo selection of x using ζ is to equate the probability that ζ is in the interval $[0, \zeta_1]$ with the probability that x is in the interval $[a, x_1]$. In Fig. 4.3, we are equating the shaded area depicting the integral of

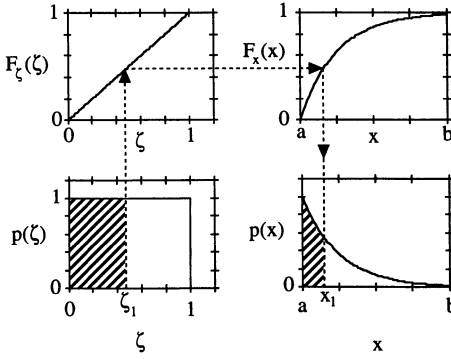


Figure 4.3. Sampling of random variables using a random number ζ . The probability density function, $p(\zeta)$, maps onto the probability density function, $p(x)$, via the distribution functions, $F_\zeta(\zeta)$ and $F_x(x)$. The shaded areas under the $p(\zeta)$ and $p(x)$ curves are equal.

$p(x)$ over $[0, x_1]$ with the area depicting the integral $p(\zeta)$ over $[0, \zeta_1]$. Keep in mind that the total areas under the curves $p(x)$ and $p(\zeta)$ each equal unity, as is appropriate for probability density functions. The result is a one-to-one mapping between the upper boundaries ζ_1 and x_1 based on the equality of the shaded areas in Fig. 4.3. In other words, we have equated $F_x(x_1)$ with $F_\zeta(\zeta_1)$. For generality, we replace the variables, ζ_1 and x_1 , by the continuous variables ζ and x :

$$F_\zeta(\zeta) = F_x(x) \quad (4.4)$$

or

$$\zeta = \int_a^x p(x) dx \quad (4.5)$$

where ζ is a random number between $[0, 1]$. Equation (4.5) is the basic equation for sampling a nonuniformly distributed $p(x)$ based on a randomly generated variable ζ . To illustrate the use of Eq. (4.5), the following sections describe the selection of stepsize, s , the deflection angle, θ , and the azimuthal angle, ψ .

4.2.1. Selecting Stepsize, s

The stepsize of the photon is calculated based on the sampling of the probability for the photon's free path, $s \in [0, \infty)$. According to the definition of the absorption and scattering coefficients, the probability of interaction (either absorption or scattering) with the medium per unit pathlength in the interval $[s_1, s_1 + ds_1]$ is $\mu_t ds_1$. The function of photon interactions in the ds_1 interval corresponds to the normalized gradient of transmission relative to ds_1 . That is,

$$\frac{-dT(s_1)}{T(s_1) ds_1} = \mu_t = \mu_a + \mu_s \quad (4.6)$$

where μ_a is the absorption coefficient, μ_s is the scattering coefficient, and μ_t is the total attenuation coefficient equal to $\mu_a + \mu_s$. All units are in cm^{-1} . Rearranging Eq. (4.6) and integrating it over the range $[0, s_1]$, one obtains the exponential distribution:

$$T(s_1) = \exp(-\mu_t s_1) \quad (4.7)$$

Note that $T(s_1)$ represents the probability of occurrence of photon pathlengths larger than s_1 which is represented by $P\{s \geq s_1\}$. Equation (4.7) can be rearranged to yield the cumulative distribution function of free path s :

$$P\{s < s_1\} = 1 - \exp(-\mu_t s_1) \quad (4.8)$$

Now the probability density function, $p(s_1)$, for free path s is expressed by

$$p(s_1) = \frac{dP\{s < s_1\}}{ds_1} = \mu_t \exp(-\mu_t s_1) \quad (4.9)$$

Now we apply Eq. (4.5):

$$\begin{aligned} \zeta &= \int_0^s p(s) ds = \int_0^s \mu_t \exp(-\mu_t s) ds \\ &= 1 - \exp(-\mu_t s) \end{aligned} \quad (4.10)$$

The right-hand sides of both Eqs. (4.10) and (4.8) are the same and the reader may wonder why we have gone in a logical circle. Our motive was to first establish $p(s)$, then apply Eq. (4.5). We shall follow this general procedure for selecting random variables. Rearranging Eq. (4.10) we have

$$\exp(-\mu_t s) = 1 - \zeta \quad (4.11)$$

Solving for s yields

$$s = \frac{-\ln(1 - \zeta)}{\mu_t} \quad (4.12)$$

Since $-\ln(1 - \zeta)$ is equivalent to $-\ln(\zeta)$ when ζ is a random variable in $(0, 1]$, Eq. (4.12) can be restated as

$$s = \frac{-\ln(\zeta)}{\mu_t} \quad (4.13)$$

4.2.2. Selecting Deflection Angle, θ

When a photon is scattered, the photon trajectory is deflected by an angle θ in the interval $[0, \pi]$. The probability density function that Henyey and Greenstein⁴ originally proposed for galactic light scattering approximates Mie scattering by particles comparable in size to the wavelengths of light, and is given by

$$p(\cos\theta) = \frac{1 - g^2}{2(1 + g^2 - 2g\cos\theta)^{3/2}} \quad (4.14)$$

The parameter g is called the anisotropy factor and characterizes the angular distribution of scattering. It is convenient to substitute the variable μ for the factor $\cos\theta$, such that μ is distributed in the interval $[-1, 1]$. This density function, $p(\mu)$, as proposed by Henyey and Greenstein, is interesting because the following identity holds:

$$g = \int_{-1}^{+1} p(\mu)\mu \, d\mu = \langle \mu \rangle \quad (4.15)$$

which equals the expectation value $\langle \mu \rangle$, or $\langle \cos\theta \rangle$, and defines g . Therefore, g characterizes the average amount of scattering in a medium, Eq. (4.15), but also specifies the shape of the scattering function, Eq. (4.14). The anisotropy, g , has a value between -1 and 1 . A value of 0 indicates isotropic scattering and a value near 1 indicates very forward-directed scattering. Jacques *et al.*⁵ determined experimentally that the Henyey–Greenstein function adequately describes the probability density function of scattering in tissue (dermis). Values for g range between 0.3 and 0.98 for tissues, but quite often g is ~ 0.9 in the visible spectrum.

Applying Eq. (4.5) we obtain:

$$\begin{aligned} \zeta &= \int_{-1}^{\mu} p(\mu) \, d\mu \\ &= \int_{-1}^{\mu} \frac{1 - g^2}{2(1 + g^2 - 2g\mu)^{3/2}} \, d\mu \end{aligned} \quad (4.16)$$

Solving for μ we have⁶

$$\mu = \frac{1}{2g} \left[1 + g^2 - \left(\frac{1 - g^2}{1 - g + 2g\zeta} \right)^2 \right] \quad \text{for } g \neq 0 \quad (4.17)$$

As g approaches zero, Eq. (4.17) becomes undefined. But in that limit, scattering becomes isotropic and the probability density function of Eq. (4.14) becomes $p(\mu) = 1/2$. Applying Eq. (4.5) yields

$$\begin{aligned}\zeta &= \int_{-1}^{\mu} \frac{1}{2} d\mu \\ &= \frac{1}{2} (\mu + 1)\end{aligned}\tag{4.18}$$

Solving for μ we obtain

$$\mu = 2\zeta - 1 \quad \text{for } g = 0\tag{4.19}$$

4.2.3. Selecting Azimuthal Angle, ψ

When a photon is deflected by an angle θ , we assume that the photon deflects symmetrically about the initial axis of propagation at an azimuthal ψ that is uniformly distributed within the interval $[0, 2\pi]$. Here we ignore asymmetric scattering. The probability density function, $p(\psi)$, is constant and equals $1/2\pi$. Applying Eq. (4.5) we have

$$\begin{aligned}\zeta &= \int_0^{\psi} \frac{1}{2\pi} d\psi \\ &= \frac{\psi}{2\pi}\end{aligned}\tag{4.20}$$

which gives ψ in the form

$$\psi = 2\pi\zeta\tag{4.21}$$

4.3. RULES FOR PHOTON PROPAGATION

This section presents the equations that describe photon propagation in the Monte Carlo model as applied to tissues. The treatment draws principally from Prahl *et al.*⁷ Figure 4.4 indicates the basic flowchart for one implementation of a Monte Carlo calculation that uses a weighted photon to improve the statistics of the simulation.

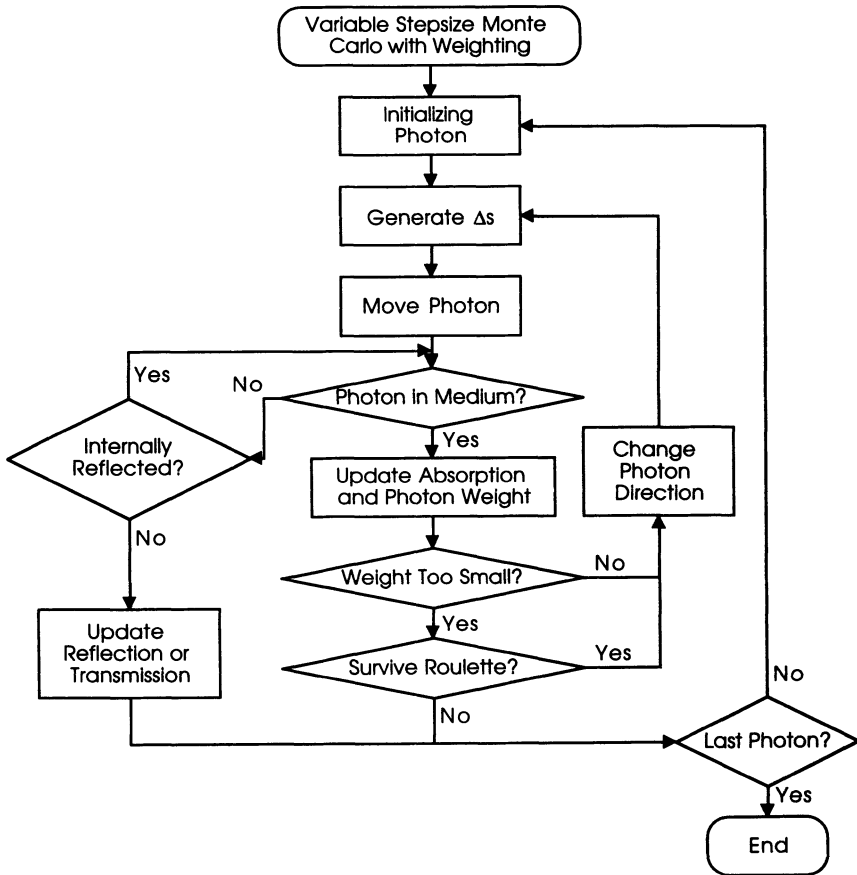


Figure 4.4. A simplified flow diagram for the Monte Carlo simulation of photon propagation. The photon is initialized with a weight of unity. The distance of the photon's step to the first interaction event is found, and the photon is moved. If the photon has left the tissue, the possibility of internal reflectance is checked. If the photon is internally reflected, then the photon position is adjusted accordingly and the program continues, otherwise the photon escapes and the event is recorded as observable reflectance (or transmittance). With each step, the photon's weight is decremented. The fraction of lost weight is added to the local element of an array associated with the position of the photon that indicates photon energy absorbed by the tissue. The remaining photon weight is then scattered statistically to achieve a new direction, and a new step is calculated. If the photon weight falls below a threshold minimum value, then roulette is played to either extinguish the photon or continue propagating the photon (with permission, Ref. 7).

4.3.1. Conventions

The details of the grid element organization for accumulating data will be delayed for later discussion in Section 4.4. Throughout this section, the arrays will simply be referenced by the location of the grid element, (x, y, z) , rather than by the indices of the grid element, $[i, j, k]$.

Throughout this section, the “equations” will often utilize an arrow (\leftarrow) to indicate the assignment of a new parameter value, a convention similar to the assignment of values in a computer programming statement.

4.3.2. Launching the Photon

Each photon is initially assigned a weight, W , equal to unity. The photon is injected orthogonally into the tissue at the origin, which corresponds to a collimated ray of incident photons. Alternative photon sources are discussed in Section 4.5.

When the photon is launched, if there is a mismatched boundary at the tissue surface, then some specular reflectance will occur. If the refractive indices of the outside medium and tissue are n_1 and n_2 , respectively, then the specular reflectance, R_{sp} , is specified as

$$R_{sp} = \frac{(n_1 - n_2)^2}{(n_1 + n_2)^2} \quad (4.22)$$

The photon weight is decremented by R_{sp} :

$$W = 1 - R_{sp} \quad (4.23)$$

The specular reflectance is stored as the parameter R_{sp} , and is used when considering total reflectance in contrast to diffuse reflectance. Subsequent discussion of reflectance refers to the diffuse reflectance due to photons that entered the tissue and later escaped.

4.3.3. Photon Stepsize, s

The stepsize of the photon, s , is calculated based on a random sampling of the probability density function for s . The computer's random number generator yields a random variable, ζ , in the interval $(0,1]$. As before, using Eq. (4.13), the sampling of s is given by

$$s = \frac{-\ln \zeta}{\mu_t} \quad (4.24)$$

where $\mu_t = \mu_a + \mu_s$. The mean free path between photon–tissue interaction

sites is $1/\mu_r$. In turbid tissues at visible and near-infrared wavelengths, μ_s is typically about 100 times greater than μ_a and the scattering coefficient dominates the prediction of s .

4.3.4. Moving the Photon

Once s is specified, the photon is ready to be moved in the tissue. The current position of the photon is specified by (x, y, z) . The current trajectory of the photon is specified by a unit vector, \mathbf{r} , which is characterized by the direction cosines (μ_x, μ_y, μ_z) , following Witt³:

$$\begin{aligned}\mu_x &= \mathbf{r} \cdot \mathbf{x} \\ \mu_y &= \mathbf{r} \cdot \mathbf{y} \\ \mu_z &= \mathbf{r} \cdot \mathbf{z}\end{aligned}\tag{4.25}$$

where \mathbf{x} , \mathbf{y} , and \mathbf{z} are unit vectors along each axis. Initially at launching, the photon position is $(0, 0, 0)$ and the trajectory is $(0, 0, 1)$. The new position of the photon is specified by (x', y', z') , and is calculated:

$$\begin{aligned}x' &= x + \mu_x s \\ y' &= y + \mu_y s \\ z' &= z + \mu_z s\end{aligned}\tag{4.26}$$

The simplicity of Eqs. (4.26) is a major reason for using Cartesian coordinates.

4.3.5. Internal Reflectance or Escape

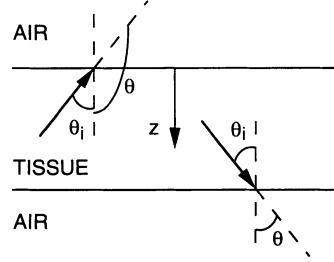
During a step, the photon may cross a boundary. For example, the photon may attempt to escape the tissue at the air/tissue interface. If this is the case, then the photon may either escape as observed reflectance (or transmittance, if a rear boundary is also included) or be internally reflected by the interface. The probability of a photon being internally reflected depends on the angle of incidence, θ_i , onto the boundary, where $\theta_i = 0$ implies orthogonal incidence. The value of θ_i is calculated (Fig. 4.5):

$$\theta_i = \cos^{-1}(|\mu_z|) = \begin{cases} \cos^{-1}(\mu_z) & \text{if } \mu_z \geq 0 \\ \pi - \cos^{-1}(\mu_z) & \text{if } \mu_z < 0 \end{cases}\tag{4.27}$$

Snell's law indicates the relationship between the angle of incidence, θ_i , the angle of transmittance, θ_t , and the refractive indices of the media from which the photon is incident, n_i , and transmitted, n_t :

$$n_i \sin \theta_i = n_t \sin \theta_t\tag{4.28}$$

Figure 4.5. Illustration of relation of θ and θ_i for the top and bottom boundaries of a tissue slab, where θ is $\cos^{-1}(\mu_z)$.



The internal reflectance, $R(\theta_i)$, is calculated by Fresnel's law^{8,9}:

$$R(\theta_i) = \frac{1}{2} \left[\frac{\sin^2(\theta_i - \theta_t)}{\sin^2(\theta_i + \theta_t)} + \frac{\tan^2(\theta_i - \theta_t)}{\tan^2(\theta_i + \theta_t)} \right] \quad (4.29)$$

A fraction, $1 - R(\theta_i)$, of the current photon weight successfully escapes the tissue as observable reflectance, and increments the local reflectance array:

$$R(x', y') \leftarrow R(x', y') + (1 - R(\theta_i))W \quad (4.30)$$

The primed coordinates, x' and y' , are used to emphasize that (x', y') refers to the position of escape, not the position of the photon. Only a fraction of the step s is taken by the photon before a portion of it successfully escapes. The actual position of escape must be calculated based on the value of this foreshortened stepsize, s' , which is

$$\begin{aligned} s' &= \frac{-z}{\mu_z} & \text{if } z' \leq 0 \\ s' &= \frac{\tau - z}{\mu_z} & \text{if } z' \geq \tau \end{aligned} \quad (4.31)$$

where τ is the thickness of tissue. Equations (4.26) are then used, substituting s' for s , to calculate the position of escape, (x', y') .

A fraction $R(\theta_i)$ of the current photon weight is internally reflected. The new photon weight is calculated:

$$W \leftarrow R(\theta_i)W \quad (4.32)$$

The photon also has a new position and trajectory. The x and y coordinates computed with Eqs. (4.26) and using the full length s do not change; only the z coordinate needs to be changed:

$$\begin{aligned} z &\leftarrow -z & \text{if } z \leq 0 \text{ (outside slab at top surface)} \\ z &\leftarrow 2\tau - z & \text{if } z \geq \tau \text{ (outside slab at bottom surface)} \end{aligned} \quad (4.33)$$

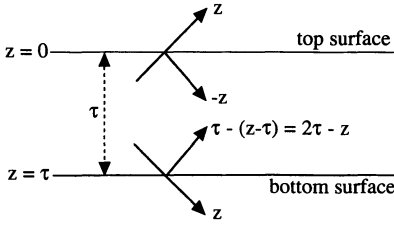


Figure 4.6. Internal reflectance. When a photon is internally reflected, the z coordinate of the photon is changed from its would-be position outside the tissue to a position within the tissue.

where τ is the thickness of the tissue slab. The geometry of this calculation is illustrated in Fig. 4.6. The new trajectory simply reverses the z component of the trajectory:

$$\mu_z \leftarrow -\mu_z \quad (4.34)$$

4.3.6. Photon Absorption

Once the photon has taken a step, some attenuation of the photon weight due to absorption by the tissue must occur. The amount of deposited photon weight, ΔQ , is calculated by

$$\Delta Q = W \frac{\mu_a}{\mu_t} \quad (4.35)$$

The current value, $Q(x, y, z)$, for the total accumulated photon weight previously deposited in the local grid element (x, y, z) is updated:

$$Q(x, y, z) \leftarrow Q(x, y, z) + \Delta Q \quad (4.36)$$

The new photon weight, W , is calculated:

$$W \leftarrow W \frac{\mu_s}{\mu_t} \quad (4.37)$$

Note that $(\mu_a/\mu_t + \mu_s/\mu_t)$ equals unity, so energy is conserved.

4.3.7. Terminating a Photon

If the photon weight, W , has been sufficiently decremented such that it falls below a threshold value (e.g., $W_{\text{threshold}} = 0.001$), then further propagation of the photon yields little information. However, proper termination must be

executed to ensure conservation of energy without skewing the distribution of photon deposition. A technique called roulette is used to terminate the photon when $W \leq W_{\text{threshold}}$. The roulette technique gives the photon one chance in m (e.g., $m = 10$) of surviving with a weight of mW . Otherwise, the photon weight is reduced to zero and the photon is terminated. A random number, ζ , in the interval $[0, 1]$ is generated by the computer. The photon weight is updated according to the following decision:

$$\begin{aligned} &\text{if } \zeta \leq 1/m \text{ then } W \leftarrow mW \\ &\text{if } \zeta > 1/m \text{ then } W = 0 \end{aligned} \quad (4.38)$$

This method conserves energy and eventually terminates photons in an unbiased manner.

4.3.8. Scattering the Photon

Once the photon has been moved and its weight decremented, the photon is ready to be scattered. A random number, ζ , is generated. The selection of the deflection angle, θ , is accomplished in terms of the $\cos\theta$ or μ as previously discussed in Eqs. (4.17) and (4.18):

$$\mu = \begin{cases} \frac{1}{2g} \left[1 + g^2 - \left(\frac{1 - g^2}{1 - g + 2g\zeta} \right)^2 \right] & \text{if } g > 0 \\ 2\zeta - 1 & \text{if } g = 0 \end{cases} \quad (4.39)$$

The photon deflection θ equals $\cos^{-1}(\mu)$.

The azimuthal angle, ψ , is calculated as previously discussed in Eq. (4.21). The selection of ψ is based on a random number, ζ :

$$\psi = 2\pi\zeta \quad (4.40)$$

Once the deflection and azimuthal angles are calculated, the new trajectory of the photon (μ'_x, μ'_y, μ'_z) is calculated from the old trajectory (μ_x, μ_y, μ_z) and the deflection angles θ and ψ ^{3,7}:

$$\begin{aligned} \mu'_x &= \frac{\sin\theta}{\sqrt{1 - \mu_z^2}} (\mu_x \mu_z \cos\psi - \mu_y \sin\psi) + \mu_x \cos\theta \\ \mu'_y &= \frac{\sin\theta}{\sqrt{1 - \mu_z^2}} (\mu_y \mu_z \cos\psi + \mu_x \sin\psi) + \mu_y \cos\theta \\ \mu'_z &= -\sin\theta \cos\psi \sqrt{1 - \mu_z^2} + \mu_z \cos\theta \end{aligned} \quad (4.41)$$

If the angle is too close to normal (i.e., $|\mu_z| > 0.99999$), then the following formulas should be used⁷:

$$\begin{aligned}\mu'_x &= \sin\theta \cos\psi \\ \mu'_y &= \sin\theta \sin\psi \\ \mu'_z &= \mu_z \cos\theta/|\mu_z|\end{aligned}\tag{4.42}$$

4.3.9. Multilayered and Complex Tissues

This is the appropriate point to mention multilayered tissue models (Fig. 4.7) and more complex models with buried cylinders (e.g., blood vessels and tubular structures) or spheres (e.g., tumors). Models can include regions of tissue or material with different optical properties and refractive index. A brief discussion of how to treat such internal boundaries follows.

Consider a photon which attempts to make a step s within tissue 1 with μ_{a1} , μ_{s1} , n_1 , but crosses a boundary into tissue 2 with μ_{a2} , μ_{s2} , n_2 after a foreshortened step s_1 . The first question asked is whether or not the photon is reflected by the refractive index mismatch. Reflection depends on the angle of incidence onto the boundary and the refractive indices, n_1 and n_2 . The question is handled in a manner similar to the above treatment of internal reflectance to yield a value for $R(\theta_i)$ using Eqs. (4.27)–(4.29). To determine whether or not the photon is reflected by the boundary or transmits into tissue 2, a random number, ζ , is generated:

$$\begin{aligned}\text{if } \zeta \leq R(\theta_i) &\text{ then the photon is reflected} \\ \text{if } \zeta > R(\theta_i) &\text{ then the photon is transmitted}\end{aligned}\tag{4.43}$$

Note that in this situation the entire photon weight is either reflected or transmitted. If the photon is reflected, then the position and trajectory are simply updated appropriately. But if the photon is transmitted into tissue 2, then the

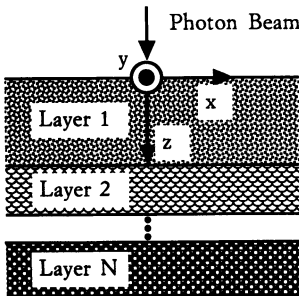


Figure 4.7. Illustration of a multilayered slab system and the Cartesian coordinate.

following procedure is followed. The photon has traveled a foreshortened step-size s_1 within tissue 1, which corresponds to a distance of $s_1\mu_{t1}$ in dimensionless units of optical depth. The photon still intends to travel a further distance of $(s - s_1)\mu_{t1}$. But this additional distance will take place in tissue 2. Therefore, the remaining stepsize, s_2 , in tissue 2 is specified as

$$s_2 = \frac{(s - s_1) \mu_{t1}}{\mu_{t2}} \quad (4.44)$$

Equations (4.26) are used, substituting s_1 for s , to calculate the foreshortened step within tissue 1. Before moving the photon in tissue 2, we need to update the directional cosines if there is a refractive index mismatch between tissues 1 and 2. The new directional cosines are¹⁰

$$\begin{aligned} \mu'_x &= \mu_x n_1/n_2 \\ \mu'_y &= \mu_y n_1/n_2 \\ \mu'_z &= \text{SIGN}(\mu_z) \cos\theta_t \end{aligned} \quad (4.45)$$

where $\text{SIGN}(\mu_z)$ returns 1 if μ_z is positive, -1 if negative. Zero μ_z is not considered here, because it means that the incident beam is parallel with the interface and there is no interface crossing; θ_t is the transmission angle in tissue 2. Then Eqs. (4.26) are again applied, substituting s_2 for s , to complete the step in tissue 2. This approach is relatively simple. Of course, we are not mentioning the hardest task, which is developing an efficient code that manages the geometry of tissue structures and detects boundary crossings.

4.4. THE DATA

4.4.1. The Basic Idea

The basic strategy of this implementation of the Monte Carlo method is to record the accumulated photon energy density, Q , in J/cc that is deposited in a local tissue volume. The local light fluence, ϕ , in J/cm² is calculated using the local absorption coefficient, μ_a , in cm⁻¹:

$$\phi = \frac{Q}{\mu_a} \quad (4.46)$$

4.4.2. The Grid Elements

The propagation of photons according to the equations in Section 4.3 is conducted using Cartesian coordinates. A choice must still be made regarding

how to store photon deposition. One must choose an array to serve as the grid element system for data acquisition of the internal distribution of Q .

Since many of our problems are symmetric around the central z axis, we have chosen a grid system in cylindrical coordinates to minimize the computer memory space required. A cylindrical coordinate system requires two variables (r, z), while a Cartesian coordinate system requires three variables (x, y, z). Also, we have chosen equally spaced grids because the resulting plots of iso-fluence contours are smooth at positions distant from the source at the origin. In contrast, logarithmically scaled grid sizes offer better resolution near the source but poor resolution at distant points. But these choices are arbitrary.

Let us organize the grid in cylindrical coordinates as an array, $Q[i, j]$, which corresponds to the accumulated energy deposition, $Q(r, z)$, in units of photon weight. Photon propagation is conducted in Cartesian coordinates of x, y , and z , as discussed previously. Energy deposition is stored in cylindrical coordinates of r and z . The coordinate r is given by

$$r = \sqrt{x^2 + y^2} \quad (4.47)$$

which always yields a positive value for r . All values of z are positive within the tissue slab. The grid element $[i, j]$ corresponds to the position (r, z) such that

$$\begin{aligned} idr &\leq r < (i + 1)dr \\ jdz &\leq z < (j + 1)dz \end{aligned} \quad (4.48)$$

If the computer language offers an INTEGER function that rounds off 2.49 to 2 and 2.50 to 3, then the following assignment statements are used:

$$\begin{aligned} i &= \text{INTEGER} \left(\frac{r}{dr} - 0.5 \right) \\ j &= \text{INTEGER} \left(\frac{z}{dz} - 0.5 \right) \end{aligned} \quad (4.49)$$

and INTEGER of a negative number equals zero.

The volume, $V(i)$, of the volume element corresponding to $[i, j]$ is calculated:

$$\begin{aligned} V(i) &= \int_{idr}^{(i+1)dr} 2\pi r \, dr \, dz \\ &= \pi[(i + 1)dr]^2 - (idr)^2 dz \\ &= (2i + 1) \pi \, dr^2 \, dz \end{aligned} \quad (4.50)$$

Note that in this cylindrical system, each volume element corresponds to an annular ring whose diameter is $\sim r$, thickness is dr , and depth is dz .

4.4.3. Converting the Raw Data to Q and ϕ

After completing a Monte Carlo simulation involving N photons (e.g., $N = 10,000$), the accumulated deposited photon weight is stored in grid elements $Q[i, j]$ in units of photon weight. This raw data is converted into energy density, $Q[i, j]$, in units of J/cm^3 by assuming that the total energy of N photons represents some value of energy, for example 1 J. In this sense, each “photon” is really a packet of photons. Then, the energy density is calculated by the following expression:

$$Q[i, j] \leftarrow \frac{Q[i, j] (1 \text{ Joule})}{NV(i)} \quad (4.51)$$

To calculate the light distribution, $\phi[i, j]$, in J/cm^2 , Eq. (4.46) is restated in terms of the arrays:

$$\phi[i, j] = \frac{Q[i, j]}{\mu_a[i, j]} \quad (4.52)$$

where $\mu_a[i, j]$ denotes the absorption coefficient of the local grid element. In a homogeneous tissue, μ_a is constant, but in complex tissue models μ_a may vary.

Consider an example. Assume that the incremental sizes of our grid system are $dz = 10 \text{ } \mu\text{m}$ and $dr = 10 \text{ } \mu\text{m}$ (or 10^{-3} cm each). The volume of the volume element at $r = 105 \text{ } \mu\text{m}$ and $z = 305 \text{ } \mu\text{m}$, which corresponds to element $[i = 10, j = 30]$, is calculated using Eq. (4.50) and equals $[(2)(10) + 1]\pi(10^{-3} \text{ cm})^3$ or 0.0660 cm^3 . Assume that this volume element has accumulated a deposited photon weight amounting to 999.9 after delivery of 10^4 photons. The energy density will equal

$$Q \leftarrow \frac{999.9 (1 \text{ Joule})}{(10^4)(0.0660 \text{ cm}^3)} = 1.51 \text{ J/cm}^3 \quad (4.53)$$

Furthermore, let us assume that the local absorption coefficient, μ_a , in that volume element was 0.5 cm^{-1} . Then the fluence of light, ϕ , in J/cm^2 is calculated:

$$\phi = \frac{Q}{\mu_a} = \frac{1.51 \text{ J/cm}^3}{0.5 \text{ cm}^{-1}} = 3.03 \text{ J/cm}^2 \quad (4.54)$$

4.4.4. Reflectance (Transmittance) Data

Recall that reflectance (or transmittance) of photons, $R(x, y)$ or $T(x, y)$, was calculated in terms of their position of escape at (x, y) . Let us choose to store the reflectance in the array $R[i]$ where i denotes the cylindrical coordinate r , as

defined in Eqs. (4.47)–(4.49). The raw data is converted to a useful form by the expression

$$R[i] \leftarrow \frac{R[i]}{N(2i + 1)\pi dr^2} \quad (4.55)$$

The units of $R[i]$ are cm^{-2} .

In general terms, $R(r)$ is the local diffuse reflectance in cm^{-2} , which expresses the fraction of the incident energy that escapes per unit area of surface. The total reflectance, R_t , is given by

$$R_t = R_{sp} + \int_0^\infty R(r) 2\pi r dr \quad (4.56)$$

where R_{sp} is the specular reflectance that occurs at photon interaction; see Eq. (4.22). Both R_t and R_{sp} are dimensionless.

4.5. VARIETIES OF SOURCES

The above treatment has considered a Monte Carlo simulation where all photons were launched at the origin perpendicular to the tissue surface. The result is essentially a narrow impulse of collimated radiation incident at the surface, which is a special case not usually encountered in the research laboratory or medical clinic. More typical types of sources are the uniform flat-field beam of finite diameter, the Gaussian beam profile, the divergent beam from an optical fiber, and a point source of fluorescence within a tissue. The propagation and data analysis equations of Sections 4.3 and 4.4 can be applied to all these cases.

Two approaches toward treatment of various launch conditions are considered here. One approach (method 1) is to distribute the N delivered photons over distributions of angle and/or position at the time of launch into the tissue. This approach is more generally applicable, and is used when modeling asymmetric heterogeneous tissue models such as a buried cylindrical blood vessel or a spherical tumor positioned off the central z axis. The disadvantage is that the simulation is run only for the distribution of radiant exposure specified at photon launching. If one wishes to calculate the distributions achieved by several beam diameters, for example, then a Monte Carlo simulation must be run for each diameter.

The second approach (method 2) is to launch photons at the origin to generate an impulse response, then convolve the resulting impulse response against various radiant exposure distributions.^{6,7,10} This approach efficiently allows subsequent consideration of a variety of source distributions of radiant exposure based on a single Monte Carlo simulation. However, the method is restricted to symmetric tissue models which allow convolution, such as homo-

geneous tissues, multiple planar layers, or a buried sphere centered on the central z axis. But buried targets such as a buried horizontal cylinder (a blood vessel) or a sphere off the central z axis (a tumor) will break the symmetry and disallow convolution. Let us compare the two methods using the examples of a collimated flat-field beam (uniform radiant exposure) and a Gaussian beam.

4.5.1. Method 1: Distributing Photons at Launch

4.5.1.1. Flat-Field Beam

Assume a collimated flat-field beam has a radius w and a total energy of 1 unit (e.g., 1 J). Since we deal with steady-state Monte Carlo simulation in this chapter, energy and power can be converted easily. The radiant exposure of the source, $S(r)$, is given

$$S(r) = \begin{cases} 1/\pi w^2 & r \leq w \\ 0 & r > w \end{cases} \quad (4.57)$$

The probability density function, $p(r)$, for radial distribution must satisfy the condition

$$\int_0^w p(r) dr = \int_0^w S(r) 2\pi r dr = 1 \quad (4.58)$$

Therefore,

$$p(r) = S(r)2\pi r = \frac{2\pi r}{\pi w^2} = \frac{2r}{w^2} \quad (4.59)$$

To randomly select an appropriate position r to launch a photon, we apply Eq. (4.5), where ζ is a random number in the interval $[0, 1]$:

$$\begin{aligned} \zeta &= \int_0^r p(r) dr \\ &= \int_0^r \frac{2r}{w^2} dr = \frac{r^2}{w^2} \end{aligned} \quad (4.60)$$

Solving for r we obtain

$$r = w\sqrt{\zeta} \quad (4.61)$$

If the tissue model is cylindrically symmetric around the z axis, then photon deposition may be stored in a two-dimensional array $Q(r,z)$, and launching

of photons may simply occur at $x = r$ and $y = 0$. The photons are launched at position $(x = w\sqrt{\xi}, y = 0)$ with a trajectory normal to the tissue surface ($\mu_x = 0, \mu_y = 0, \mu_z = 1$).

If the tissue model is asymmetric, then we cannot store our data in a cylindrically symmetric array such as $Q(r, z)$. We must store data in a larger three-dimensional array, such as $Q(x, y, z)$. Also, we must distribute the launching of photons over the area (x, y) of radiant exposure, not simply along a line (r) as we did above. Therefore, we generate a second random number, ξ_2 . The launch position of photons is

$$\begin{aligned} x &= w \sqrt{\xi} \cos(2\pi\xi_2), \\ y &= w \sqrt{\xi} \sin(2\pi\xi_2) \end{aligned}$$

4.5.1.2. Gaussian Beam

Consider the case of a Gaussian beam with a $1/e^2$ radius of w , defined as a radiant exposure, $S(r)$, with a total energy of 1 unit (e.g., 1 J), and a radial distribution that is specified:

$$S(r) = \frac{2}{\pi w^2} \exp(-2r^2/w^2) \quad (4.62)$$

which conserves energy:

$$\int_0^{\infty} S(r) 2\pi r dr = 1 \quad (4.63)$$

Comparing Eqs. (4.1) and (4.63), the probability density function, $p(r)$, is identical to $S(r)2\pi r$:

$$\begin{aligned} p(r) &= S(r)2\pi r = \frac{2}{\pi w^2} \exp(-2r^2/w^2) 2\pi r \\ &= \frac{4r}{w^2} \exp(-2r^2/w^2) \end{aligned} \quad (4.64)$$

To randomly sample $p(r)$, we apply Eq. (4.5) where ζ is a random number in the interval $[0, 1]$:

$$\begin{aligned} \zeta &= \int_0^r p(r) dr \\ &= \int_0^r \frac{4r}{w^2} \exp(-2r^2/w^2) dr \\ &= 1 - \exp(-2r^2/w^2) \end{aligned} \quad (4.65)$$

Solving for r we obtain

$$r = w \sqrt{[-\ln(1 - \xi)]/2} \quad (4.66)$$

Therefore, photons are launched at $(x = w \sqrt{-\ln(1 - \xi)/2}, y = 0)$ when the tissue model and data storage are cylindrically symmetric. When the tissue is asymmetric, photons are launched at

$$\begin{aligned} x &= w \sqrt{-\ln(1 - \xi)/2} \cdot \cos(2\pi\xi_2), \\ y &= w \sqrt{-\ln(1 - \xi)/2} \cdot \sin(2\pi\xi_2) \end{aligned}$$

where ξ_2 is a second random number.

4.5.2. Method 2: Convolution of Impulse Response

4.5.2.1. Flat-Field Beam

Now consider the second approach, initial calculation of an impulse response followed by convolution over various beam diameters. The photons are launched at the origin ($x = 0, y = 0, z = 0$) with a trajectory normal to the tissue surface ($\mu_x = 0, \mu_y = 0, \mu_z = 1$). The results are stored in cylindrical coordinates as $Q(r, z)$ in units of photon weight, then converted to units of J/cm^3 per J of delivered energy, or simply cm^{-3} , using Eq. (4.51), and finally converted to $\phi(r, z)$ in units of J/cm^2 per J of delivered energy, or simply cm^{-2} , using Eq. (4.52).

Let us assign the values of $\phi(r, z)$ to a new function $G(r, z)$ to emphasize its role as an impulse response:

$$G(r, z) = \phi(r, z) \quad (4.67)$$

The function G will be repeatedly used during subsequent convolutions to generate various distributions for $\phi(r, z)$ that depend on the radiant exposure, $S(r)$.

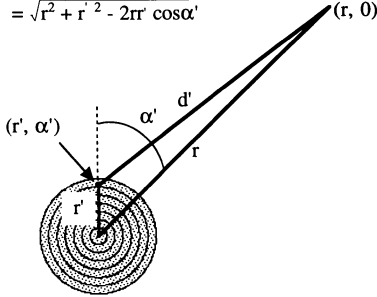
Convolution of the impulse response G against the radiant exposure S in cylindrical coordinates is illustrated in Fig. 4.8, and is specified by the expression

$$\phi(r, z) = \int_0^w S(r') \left[\int_0^{2\pi} G(\sqrt{r^2 + r'^2 - 2rr'\cos\alpha'}, z) d\alpha' \right] r' dr' \quad (4.68)$$

where w is the radius of the source, while α' is the angle between the vector

A

$$d' = \sqrt{r^2 + r'^2 - 2rr' \cos \alpha'}$$



B

$$d'' = \sqrt{r^2 + r''^2 - 2rr'' \cos \alpha''}$$

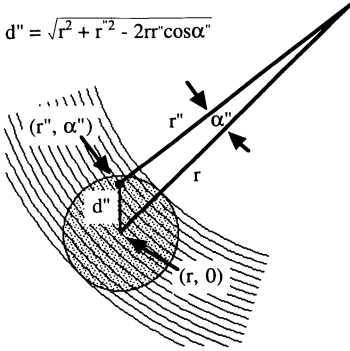


Figure 4.8. Coordinates system for convolution of impulse response, G , over the source function, S (stippled region). The thin lines indicate the rings of integration during convolution in cylindrical coordinates. The two coordinate systems shown are equivalent. (A) The origin is at the center of the source. The observation point is at $(r, 0)$. The convolution involves $S(r')$ and $G(d')$. (B) The origin is at the point of observation. The center of the source is at $(r'', 0)$. The convolution involves $S(d'')$ and $G(r'')$.

from the origin to a source point (r', α') and the vector from the origin to an observation point $(r, 0)$. Although G depends on z , the convolution is evaluated completely for one desired depth, so z is a constant during each integral evaluation. The units of G are cm^{-2} , the units of S are J/cm^2 , and the double integration yields area in units of cm^2 . Therefore, the resulting ϕ is in units of J/cm^2 .

There is a symmetry to this convolution which simplifies numerical evaluation. The cylindrical coordinate system may be transformed, as depicted in Fig. 4.8B, which allows Eq. (4.68) to be restated:

$$\phi(r, z) = \int_{w-r}^{w+r} G(r'', z) \left[\int_0^{2\pi} S(\sqrt{r^2 + r''^2 - 2rr'' \cos \alpha''}) d\alpha'' \right] r'' dr'' \quad (4.69)$$

The advantage of the transformed coordinate system is that the integral within the brackets becomes independent of depth z because S is independent of z . Therefore, a single evaluation of the bracketed term can be used repeatedly for each of the many depths, z , which are considered. In contrast, the bracketed

term in Eq. (4.68) requires reevaluation for each depth z that is considered because G depends on z .

The transformation is illustrated in Fig. 4.8. The first coordinate system has its origin at the center of the source, as in Fig. 4.8A and Eq. (4.68). The point of observation is at $(r, 0)$. An incremental region of source is located at (r', α') and has a value $S(r')$. The distance between the source point and observation point is d' , equal to $\sqrt{r^2 + r'^2 - 2rr'\cos\alpha'}$. The limits of integration range from zero to w , which is the radius of the source.

The second coordinate system has its origin at the center of the point of observation, as in Fig. 4.8B and Eq. (4.69.) The source is centered at $(r, 0)$. The incremental region of source is located at (r'', α'') and has a value $S(d'')$, where d'' equals $\sqrt{r^2 + r''^2 - 2rr''\cos\alpha''}$. The distance between the source point and observation point is r'' . The limits of integration range from $w - r$ to $w + r$, which are the minimum and maximum distances between a source point and the observation point. Note, however, that much of the region of integration lies outside the source and therefore the value of S in the integrand is zero.

In the original coordinate system (Fig. 4.8A), the uniform flat-field beam provides a source of radiant exposure, $S(r')$, that is specified:

$$S(r') = \begin{cases} \frac{P}{\pi w^2} & r' \leq w \\ 0 & r' > w \end{cases} \quad (4.70)$$

where P is the total power of the laser beam. In the transformed coordinate system (Fig. 4.8B), the solution for $\phi(r, z)$ is conveniently summarized by re-statement of Eq. (4.69):

$$\phi(r, z) = \int_{w-r}^{w+r} G(r'', z) Q(r, r'') 2\pi r'' dr'' \quad (4.71)$$

where $Q(r, r'')$ equals the integration within the bracket in Eq. (4.69) divided by 2π :

$$\begin{aligned} Q(r, r'') &= \frac{1}{2\pi} \int_0^{2\pi} S(\sqrt{r^2 + r''^2 - 2rr''\cos\alpha''}) d\alpha'' \\ &= \begin{cases} \frac{P}{\pi w^2} & r + r'' \leq w \\ \frac{\alpha''}{\pi} \left(\frac{P}{\pi w^2} \right) & |r - r''| < w \text{ or } w < r + r'' \\ 0 & |r + r''| > w \end{cases} \end{aligned} \quad (4.73)$$

where

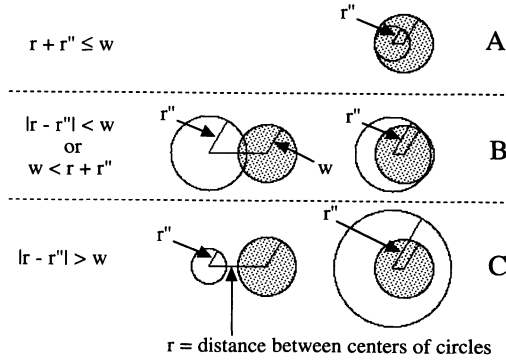


Figure 4.9. Convolution for a uniform laser beam. The source is a circular laser beam with radius w (stippled region). The observation point is at the center of the second circle (not stippled) with radius r'' . The convolution using the coordinate system of Fig. 4.5B involves integration over all possible values of r'' . Three situations arise. (A) The ring of integration with radius r'' is completely within the source. (B) The ring of integration is partially within the source. (C) The ring of integration never intersects the source. Equation (4.73) lists the forms of the integrand for these three situations during the convolution.

$$\alpha'' = \cos^{-1} \left(\frac{r^2 + r''^2 - w^2}{2rr''} \right) \quad (4.74)$$

The three situations specified in Eq. (4.73) are illustrated in Fig. 4.9.

4.5.2.2. Gaussian Beam

The solution for a Gaussian beam profile was derived by Prahl.⁶ The parameter w indicates the $1/e^2$ radius of the beam; see Eq. (4.62). The convolution is given by

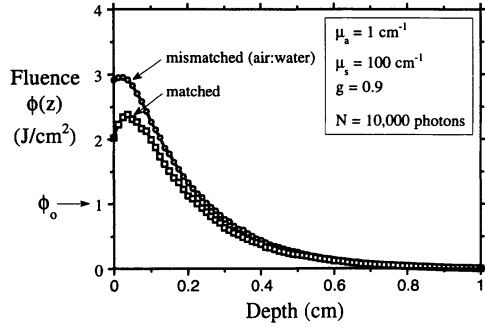
$$\phi(r, z) = \frac{2P}{\pi w^2} \exp[-2(r/w)^2] \int_0^\infty G(r'', z) \exp[-2(r''/w)^2] I_0\left(\frac{4rr''}{w^2}\right) 2\pi r'' dr'' \quad (4.75)$$

where I_0 is a zero-order modified Bessel function.

4.6. EXAMPLES

Figure 4.10 illustrates the one-dimensional distribution of light as a function of depth along the central z axis within a simulated tissue which is pro-

Figure 4.10. Fluence distribution versus depth, for matched versus mismatched surface boundary condition. An aqueous phantom tissue slab 1-cm thick is either matched or mismatched ($n_{\text{air}}:n_{\text{water}} = 1:1.33$). This one-dimensional solution is appropriate for the $\phi(z)$ along the central axis when a very large beam diameter is used, such that edge losses do not affect the result. The radiant exposure, ϕ_0 , is 1 J/cm². The matched condition allows light to escape the tissue more easily, in contrast to the mismatched boundary which internally reflects about half the photons that strike the boundary as they attempt to escape.



duced by a broad beam of flat-field irradiance. The optical properties are $\mu_a = 1 \text{ cm}^{-1}$, $\mu_s = 100 \text{ cm}^{-1}$, and $g = 0.9$, and the tissue thickness is 1 cm. Two calculations were conducted, one with a matched boundary condition at front and rear and one with a mismatched boundary condition (1:1.33, or an air/water interface) at front and rear. Each computation involves 10,000 photons and the results are stored in a cylindrical coordinate system of grid elements. The size of the grid elements is $dz = 50 \text{ }\mu\text{m}$ and $dr = 100 \text{ }\mu\text{m}$. The impulse response has been convolved over a sufficiently large source such that the diffusion losses at the edge of the beam do not affect the solution $\phi(z)$ along the central z axis. Notice that the matched boundary condition causes the fluence near the surface to drop due to escaping photons. In contrast, the mismatched boundary condition acts like a partially reflective mirror ($\sim 50\%$) that mitigates the loss of fluence near the surface.

Figure 4.11 plots the radial dependence of local reflectance, $R(r)$, versus radial position, r . The two boundary conditions and optical properties of Fig. 4.10 are used. The beam diameter is 1 mm. Note that the matched boundary condition allows greater reflectance than the mismatched boundary. Again, the mismatched boundary is acting as a partially reflective mirror which reduces photon escape. The specular reflectance that occurs during the mismatched condition is indicated by a discontinuity in $R(r)$ at the edge of the beam. The total reflectance, R_r , is 0.466 and 0.266 for the matched and mismatched conditions, respectively.

Figure 4.12 illustrates the internal distribution for a small- versus large-diameter flat-field beam, for the same optical properties as in Fig. 4.10. The total beam energy is the same for both cases. The plots are achieved by convolution of the computed impulse response against two source beam distributions, one small (0.5-mm diameter) and one large (6-mm diameter). Isofluence lines

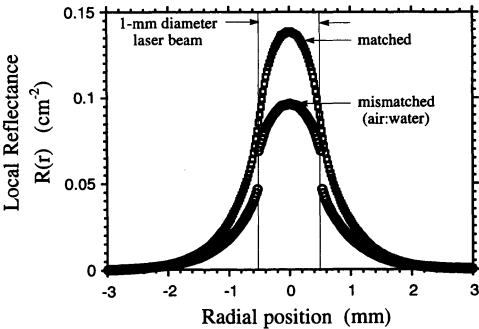


Figure 4.11. Radial distribution of the local reflectance, $R(r)$. The total reflectance equals the integral of the local reflectance: $R_t = \int_0^\infty R(r) 2\pi r dr$. Note that the mismatched boundary condition yields a lower $R(r)$ than the matched boundary condition, because the mismatched boundary internally reflects about 1/2 the photons attempting to escape the tissue. The values of R_t are 0.466 and 0.266 for matched and mismatched conditions, respectively. Also,

note the discontinuity in $R(r)$ at the edges of the incident beam, due to the specular reflectance (0.020) in the directly irradiated area.

are plotted for 10, 1, and 0.1 J/cm². Note that far from the source, the fluences are similar for both small and large beam irradiation, since the total energy is the same. But near the source, the small beam achieves very high fluences and the large beam achieves only modest fluences.

4.7. CHECKING YOUR MONTE CARLO RESULTS

Monte Carlo is not difficult to implement in any computer language, but it is easy to make a numerical mistake during the programming. Therefore, we will provide some standard test data (Table 4.1) for you to check your numerical results in case you write your own code. More examples can be found in the extensive table in Chapter 5 and elsewhere.^{6,10}

Table 4.1. Some Standard Test Data Collected from References^a

Source	n	d (cm)	μ_a (cm ⁻¹)	μ_s (cm ⁻¹)	g	R_d	T_t
van de Hulst ¹	1	0.02	10	90	0.75	0.09739	0.66096
Giovanelli ¹²	1.5	∞	10	90	0	0.2600	0

^a n is the relative refractive index of the turbid medium. d is the thickness. μ_a and μ_s are the absorption and scattering coefficients. g is the anisotropy. The computed results are R_d and T_t , which are the diffuse reflectance and total transmittance, respectively. When d is ∞ , the medium is semi-infinite.

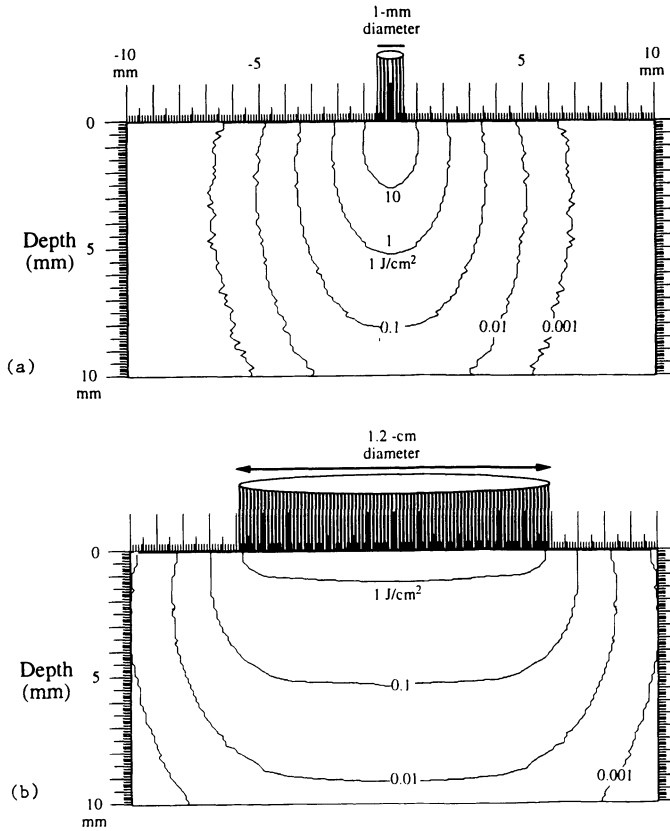


Figure 4.12. Internal fluence distribution for narrow-beam versus broad-beam radiant exposure. (a) 1-mm-diameter flat-field beam. (b) 1.2-mm-diameter flat-field beam. Isofluence lines of 10, 1, 0.1, and 0.01 J/cm² are indicated. The total beam energy is 100 mJ for both cases. The surface boundary is mismatched (1:1.33). Note that near the source the confinement of the energy in a narrow beam yields high fluences, compared to the low fluences of a distributed broad beam. But far from the source, both beams yield similar fluence distributions because the total beam energy is the same. ($\mu_a = 1 \text{ cm}^{-1}$, $\mu_s = 10 \text{ cm}^{-1}$, $g = 0.9$.)

ACKNOWLEDGMENTS

We wish to acknowledge the contributions of Scott A. Prahl, Marleen Keijzer, Iyad Saidi, and A. J. Welch, who have been our collaborators during the development of these Monte Carlo simulations. This work was supported by the NIH (R29-HL45045) and the Department of the Navy (N00015-91-J-1354).

4.8. REFERENCES

1. Cheong WF, Prah SA, Welch AJ. "A review of the optical properties of biological tissues," *IEEE J Quantum Electronics* **26**: 2166–2185 (1990).
2. Cashwell ED, Everett CJ. *A Practical Manual on the Monte Carlo Method for Random Walk Problems*, Pergamon Press, New York (1959).
3. Witt AN. "Multiple scattering in reflection nebulae I: A Monte Carlo approach," *Astrophys. J. Suppl. Ser.* **35**: 1–6 (1977).
4. Henyey LG, Greenstein JL. "Diffuse radiation in the galaxy," *Astrophys. J.* **93**: 70–83 (1941).
5. Jacques SL, Alter CA, Prah SA. "Angular dependence of HeNe laser light scattering by human dermis," *Lasers Life Sci.* **1**: 309–334 (1987).
6. Prah SA. "Calculation of light distributions and optical properties of tissue," Ph.D. Dissertation, Department of Biomedical Engineering, University of Texas at Austin (1988).
7. Prah SA, Keijzer M, Jacques SL, Welch AJ. "A Monte Carlo model of light propagation in tissue," in *Dosimetry of Laser Radiation in Medicine and Biology*, SPIE Institute Series IS **5**: 102–111 (1989).
8. Born M, Wolf E. *Principles of Optics: Electromagnetic Theory of Propagation, Interference and Diffraction of Light*, 6th corrected ed., Pergamon Press. New York (1986).
9. Hecht E. *Optics*, 2nd ed., Addison-Wesley, Reading, MA (1987).
10. Wang LH, Jacques SL. *Monte Carlo Modeling of Light Transport in Multi-layered Tissues in Standard C*, University of Texas / M. D. Anderson Cancer Center, 1992. The software is available on our anonymous ftp site at laser.mda.uth.tmc.edu or through e-mails to lihong@laser.mda.uth.tmc.edu or slj@laser.mda.uth.tmc.edu, or by writing to us at Laser Lab-17, UTMD Anderson Cancer Center, 1515 Holcombe Blvd., Houston, TX 77030.
11. Hulst, HC van de. *Multiple Light Scattering*, Vol. II, Academic Press, New York (1980).
12. Giovanelli RG, "Reflection by semi-infinite diffusers," *Opt. Acta* **2**: 153–162 (1955).